Propulsion and Power Research 2016;5(1):22–33

HOSTED BY

ELSEVIER

http://ppr.buaa.edu.cn/

Propulsion and Power Research

www.sciencedirect.com

ORIGINAL ARTICLE

Nozzle geometry variations on the discharge coefficient

M.M.A. Alam[a,*], T. Setoguchi[a], S. Matsuo[b], H.D. Kim[c]

[a]*Institute of Ocean Energy, Saga University (IOES), 1, Honjo, Saga-shi, Saga 840-8502, Japan*
[b]*Department of Advanced Technology Fusion, Saga University, Japan*
[c]*Department of Mechanical Engineering, Andong National University, Korea*

Received 14 February 2014; accepted 16 November 2015
Available online 12 February 2016

KEYWORDS

Boundary layer;
Compressible flow;
Reynolds-averaged Navier–Stokes (RANS);
Shear layer;
Sonic lines;
Supersonic core

Abstract Numerical works have been conducted to investigate the effect of nozzle geometries on the discharge coefficient. Several contoured converging nozzles with finite radius of curvatures, conically converging nozzles and conical divergent orifices have been employed in this investigation. Each nozzle and orifice has a nominal exit diameter of 12.7×10^{-3} m. A 3rd order MUSCL finite volume method of ANSYS Fluent 13.0 was used to solve the Reynolds-averaged Navier–Stokes equations in simulating turbulent flows through various nozzle inlet geometries. The numerical model was validated through comparison between the numerical results and experimental data. The results obtained show that the nozzle geometry has pronounced effect on the sonic lines and discharge coefficients. The coefficient of discharge was found differ from unity due to the non-uniformity of flow parameters at the nozzle exit and the presence of boundary layer as well.

1. Introduction

Nozzles are found encountering in a wide variety of engineering applications, mainly to generate jets [1–4], flow metering [5–7], and sprays [8,9]. The accurate prediction of the compressible nozzle flows is still challenging for the aerodynamicist, and achieves increasing importance since

*Corresponding author. Tel.: (880) 8043156244.
E-mail address: dralam@me.saga-u.ac.jp (M.M.A. Alam).

Peer review under responsibility of National Laboratory for Aeronautics and Astronautics, China.

http://dx.doi.org/10.1016/j.jppr.2016.01.002

Nomenclature

a	sound speed (unit: m/s)
A_e	area at nozzle exit (unit: m^2)
C_d	discharge coefficient
C_p	specific heat at constant pressure (unit: J/(kg · K))
D_e	diameter at nozzle exit (unit: m)
D_m	diameter of Mach disk (unit: m)
E	total energy per unit mass (unit: J/kg)
$\boldsymbol{F}$	inviscid flux vectors
$\boldsymbol{G}$	viscous flux vectors
H	total enthalpy per unit mass (unit: J/kg)
$\boldsymbol{H}$	vector for source terms
i	unit vector in the x-direction
j	unit vector in the y-direction
k	unit vector in the z-direction
k	turbulent kinetic energy per unit mass (unit: J/kg)
l_0	location of minimum jet section (unit: m)
L_m	location of Mach disk (unit: m)
L_s	length of supersonic core (unit: m)
$\dot{m}$	mass flow rate (unit: kg/s)
M	Mach number
p	pressure (unit: Pa)
q	heat flux (unit: W/m^2)
$\boldsymbol{Q}$	dependent vector of primary variables
r	radius (unit: m)
R	radius of curvature (unit: m)
Re	Reynolds number
T	temperature (unit: K)
U_r	reference velocity (unit: m/s)
w	electromagnetic energy density (unit: J/m^3)
u_i, u_j	Cartesian mean velocity components (unit: m/s)
v_x, v_y, v_z	Cartesian velocity components in x-, y- and z-directions (unit: m/s)

Greek symbols

β	conic divergent angle (unit: degree)
δ	boundary layer thickness (unit: m)
δ_{sh}	shear layer thickness (unit: m)
γ	ratio of specific heats
μ	dynamic viscosity (unit: Pa · s))
υ	kinematic viscosity (unit: m^2/s)
θ	conic convergent angle (unit: degree)
ρ	density (unit: kg/m^3)
$\mathfrak{R}$	gas constant (unit: J/(kmol · K))
τ	shear stress (unit: Pa)
ω	specific dissipation rate (unit: s^{-1})

Subscripts

0	stagnation point
b	ambient
t	turbulent
x	x-coordinate
y	y-coordinate
x	z-coordinate

the nozzle performance is significantly influenced by its inlet geometry. The flow emanating from nozzle exit serves as the initial conditions for the downstream jet flows. Thus, the studies on nozzle geometric effect are becoming a major interest for compressible and incompressible nozzle flows.

Several works reported information on aerodynamic features of jets and flow with various inlet-boundary conditions and nozzle geometries. Matsuo et al. [10] performed numerical study to investigate the effect of nozzle geometry on the sonic line and characteristics of the supersonic air jets. Two contoured converging nozzles, two conically converging sharp-edged nozzles (45° and 75°) and a sharp-edged orifice were employed in their study. Otobe et al. [11] investigated the near-field structure of highly underexpanded sonic jets using three nozzle geometries (cylindrical straight nozzle, 75° convergence conical nozzle and 45° divergent orifice), and they proposed an empirical relation of diameter of Mach disk in terms of the pressure ratio, regardless of the nozzle geometry. Menon and Skews [12] conducted a numerical study on underexpanded sonic jets issuing from nozzles with contoured inlet, 45° conical inlet and an orifice inlet under a range of pressure ratio between 2 and 10. Hatanaka and Saito [13] conducted experimental and numerical studies to investigate the effect of nozzle geometry on the structure of supersonic free jets for three simple nozzle geometries over a wide range of pressure ratios up to 90. However, most of the above research works concentrated mainly on the shock and Mach characteristics of jets. In another study, Yu et al. [14] performed numerical simulations to investigate the effects of geometry variations on flow through nozzles. Four nozzle configurations were considered in the study: a baseline nozzle and three modified (extended, grooved and ringed) nozzles. The turbulence characteristics of incompressible flow through nozzles at Reynolds number of approximately 50,000 were investigated in their study. Only very few studies have reported, till date, on the performance of nozzle in terms of discharge coefficients. Hebber et al. [15] conducted an analytical study to obtain a simple, explicit and analytical expression for the discharge coefficients of conical convergent nozzle operating under varying pressure ratios. Cruz-Maya et al. [16] performed study to characterize the discharge coefficients in the venturi sonic nozzle considering the viscous and multidimensional effects of the fluid flow as uncoupled phenomenon.

Since the main purpose of this research is to investigate the effect of nozzle geometries on the performance in terms of discharge coefficients, five cylindrical, four conical convergent nozzles and eight conical divergent orifices with varying radius of curvatures, convergent and divergent angles, respectively, have been used. Sonic lines and their inflections were analyzed to examine the effect of flow parameter at nozzle exit on the discharge coefficient. Based upon the computed results, the nozzle geometry has

significant influences on the discharge coefficient, profile of sonic lines and on the nozzle downstream flow features. Jet boundaries, shear layers and lengths of supersonic core of jets were investigated to clarify the performance of nozzles on the downstream flows.

2. Numerical model and computational methodology

2.1. Governing equations

Computational fluid dynamics (CFD) investigations were performed to simulate the turbulent flows through nozzle with various geometries. The flow under study was treated as compressible, viscous and supersonic at underexpanded conditions. The governing equations used in the present computations are axisymmetric, compressible Reynolds averaged Navier–Stokes (RANS) equations [17], given by:

$$\boldsymbol{\Gamma}\frac{\partial}{\partial t}\int_V \boldsymbol{Q}dV + \oint [\boldsymbol{F}-\boldsymbol{G}]\cdot \; d\boldsymbol{A} = \int_V \boldsymbol{H}dV \tag{1}$$

where, $\boldsymbol{F}$ and $\boldsymbol{G}$ are the inviscid and viscous flux vectors in standard conservation form, $\boldsymbol{Q}$ is the dependent vector of primary variables, and the vector $\boldsymbol{H}$ contains source terms.

$$\boldsymbol{F} = \left[\rho v, \rho v v_x + p\hat{i}, \rho v v_y + p\hat{j}, \rho v v_z + p\hat{k}, \rho v H\right]^{\mathrm{T}} \tag{2}$$

$$\boldsymbol{G} = \left[0, \tau_{xi}, \tau_{yi}, \tau_{zi}, \tau_{ij}v_j + q\right]^{\mathrm{T}} \tag{3}$$

$$\boldsymbol{Q} = \left[p, v_x, v_y, v_z, T\right]^{\mathrm{T}} \tag{4}$$

Here ρ, v, and p are the density, velocity, and pressure of the fluid, respectively. τ is the viscous stress tensor, and q is the heat flux. In the above equations, H is the total enthalpy per unit mass and is related to the total energy E by $H = E + p/\rho$, where E includes both internal and kinetic energies. The preconditioning matrix $\boldsymbol{\Gamma}$ is included in Eq. (1) to provide an efficient solution of the present axisymmetric compressible flow. This matrix is given by:

$$\boldsymbol{\Gamma} = \begin{bmatrix} \theta & 0 & 0 & 0 & \rho_T \\ \theta v_x & \rho & 0 & 0 & \rho_T v_x \\ \theta v_y & 0 & \rho & 0 & \rho_T v_y \\ \theta v_z & 0 & 0 & \rho & \rho_T v_x \\ \theta H - \delta & \rho v_x & \rho v_y & \rho v_z & \rho_T H + \rho C_p \end{bmatrix} \tag{5}$$

where ρ_T is the derivative of density with respect to temperature at constant pressure. $\delta = 1$ for an ideal gas and $\delta = 0$ for an incompressible fluid. The parameter θ is defined as:

$$\theta = \frac{1}{U_r^2} - \left(\rho_T H + \rho C_p\right) \tag{6}$$

In Eq. (6), the reference velocity U_r is chosen such that the eigenvalues of the system remain well conditioned with respect to the convective and diffusive timescales and C_p is the specific heat at constant pressure.

To close governing equations, the k–ω SST (shear stress transport) which is a two equation eddy-viscosity turbulence model [18–20] were employed in the computation. This turbulence model is an effective blend of the robust and accurate formulation of the Wilcox's k–ω model in the near-wall region with the free-stream independence of the k–ε model in the far field. The turbulent kinetic energy k and the specific dissipation rate ω are determined by the following transport equations.

$$\frac{\partial}{\partial t}(\rho k) + \frac{\partial}{\partial x_i}(\rho k u_i) = \frac{\partial}{\partial x_j}\left(\Gamma_k \frac{\partial k}{\partial x_j}\right) + \tilde{G}_k - Y_k \tag{7}$$

$$\frac{\partial}{\partial t}(\rho \omega) + \frac{\partial}{\partial x_i}(\rho \omega u_i) = \frac{\partial}{\partial x_j}\left(\Gamma_k \frac{\partial \omega}{\partial x_j}\right) + G_\omega - Y_\omega + D_\omega \tag{8}$$

In these equations, $\tilde{G}_k$ represents the generation of turbulence kinetic energy due to mean velocity gradients, G_ω represents the generation of ω, D_ω is the cross-diffusion term. σ_k and σ_ω are the turbulent Prandtl numbers for k and ω, respectively, and given by;

$$\sigma_k = \frac{1}{F_1/\sigma_{k,1} + (1-F_1)/\sigma_{k,2}} \tag{9}$$

and

$$\sigma_\omega = \frac{1}{F_1/\sigma_{\omega,1} + (1-F_1)/\sigma_{\omega,2}} \tag{10}$$

The turbulent viscosity μ_t is computed as;

$$\mu_t = \frac{\rho k}{\omega}\frac{1}{\max\left[1/\alpha^*,\ SF_2/\alpha_1/\omega\right]} \tag{11}$$

where S is strain rate magnitude, defined as $S \equiv \sqrt{2S_{ij}S_{ij}}$ and $S_{ij} = \frac{1}{2}\left(\frac{\partial u_j}{\partial x_i} + \frac{\partial u_i}{\partial x_j}\right)$, $\alpha = \frac{\alpha_\infty}{\alpha^*}\left(\frac{\alpha_0 + Re_t/R_\omega}{1 + Re_t/R_\omega}\right)$, and $Re_t = \frac{\rho k}{\mu\omega}$.

Blending functions F_1 and F_2 are given by;

$$F_1 = \tanh\left(\Phi_1^4\right) \tag{12}$$

$$\Phi_1 = \min\left[\max\left(\frac{\sqrt{k}}{0.09\omega y},\ \frac{500\mu}{\rho y^2 \omega}\right), \frac{4\rho k}{\sigma_{\omega,2} D_\omega^+ y^2}\right] \tag{13}$$

$$D_\omega^+ = \max\left[2\rho\frac{1}{\sigma_{\omega,2}}\frac{1}{\omega}\frac{\partial k}{\partial x_j}\frac{\partial \omega}{\partial x_j},\ 10^{-10}\right] \tag{14}$$

and

$$F_2 = \tanh\left(\Phi_2^2\right) \tag{15}$$

$$\Phi_2 = \max\left[2\frac{\sqrt{k}}{0.09\omega y},\ \frac{500\mu}{\rho y^2 \omega}\right] \tag{16}$$

where y is the distance to the next surface and D_ω^+ is the positive portion of the cross-diffusion term. The cross-diffusion term D_ω is defines as;

$$D_\omega = 2(1-F_1)\rho\sigma_{\omega,2}\frac{1}{\omega}\frac{\partial k}{\partial x_j}\frac{\partial \omega}{\partial x_j} \tag{17}$$

Model constants are given as;

$$\sigma_{k,1} = 1.176, \quad \sigma_{\omega,1} = 2.0, \quad \sigma_{k,2} = 1.0, \quad \sigma_{\omega,2} = 1.168$$

$\alpha_1 = 0.31, \quad \beta_{i,1} = 0.075, \quad \beta_{i,2} = 0.0828$

$\alpha^*_\infty = 1, \quad \alpha_\infty = 0.52, \quad \alpha_0 = \frac{1}{9}, \quad \beta^*_\infty = 0.09$

$R_k = 6, \quad R_\omega = 2.95, \quad \zeta^* = 1.5$

2.2. Numerical methods

The density-based algorithm in ANSYS Fluent 13.0 [17] was used to solve the preconditioned governing equations. A fully implicit method was implemented on the present spatial domain. The convective fluxes were formulated using the Roe's flux difference splitting scheme [21], and the 3rd order accuracy of this scheme was conceived from the original MUSCL (monotonic upstream-centered scheme for conservation laws) [22] finite volume scheme that is a blend of central differencing and second-order upwind schemes, in which the physical domain is subdivided into numerical cells, and the integral equations were applied to each cell. Second-order central difference scheme was used for viscous terms.

2.3. Computational conditions

Schematics of the computational domain used in the present study are illustrated in Figure 1. Nozzles with the following geometry variations were studied:

(1) Addy [23] nozzle which is a cylindrical straight nozzle is composed of a convergent curved entrance wall having radius of curvature $R = D_e$ followed by straight wall with a length of $0.4D_e$ (Figure 2(a)).

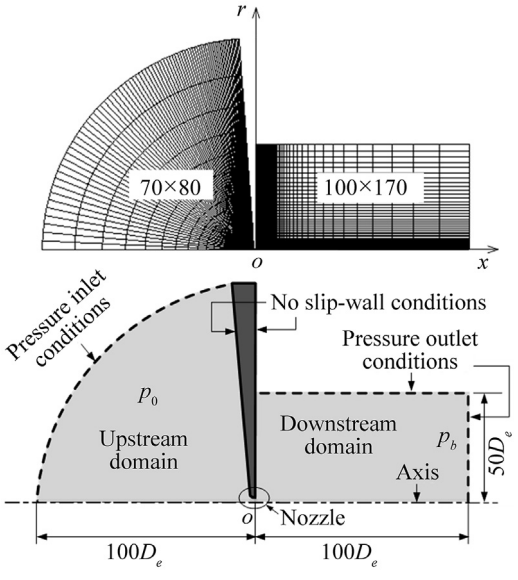

Figure 1 Schematics of computational domain and boundary conditions.

(2) Cylindrical nozzles with variable radius of curvatures $R = 6$, 12, 18, 24 and 30 mm (Figure 2(b)).
(3) Conical nozzles with convergence angles $\theta = 30^\circ$, 45°, 60° and 75° (Figure 2(c)).

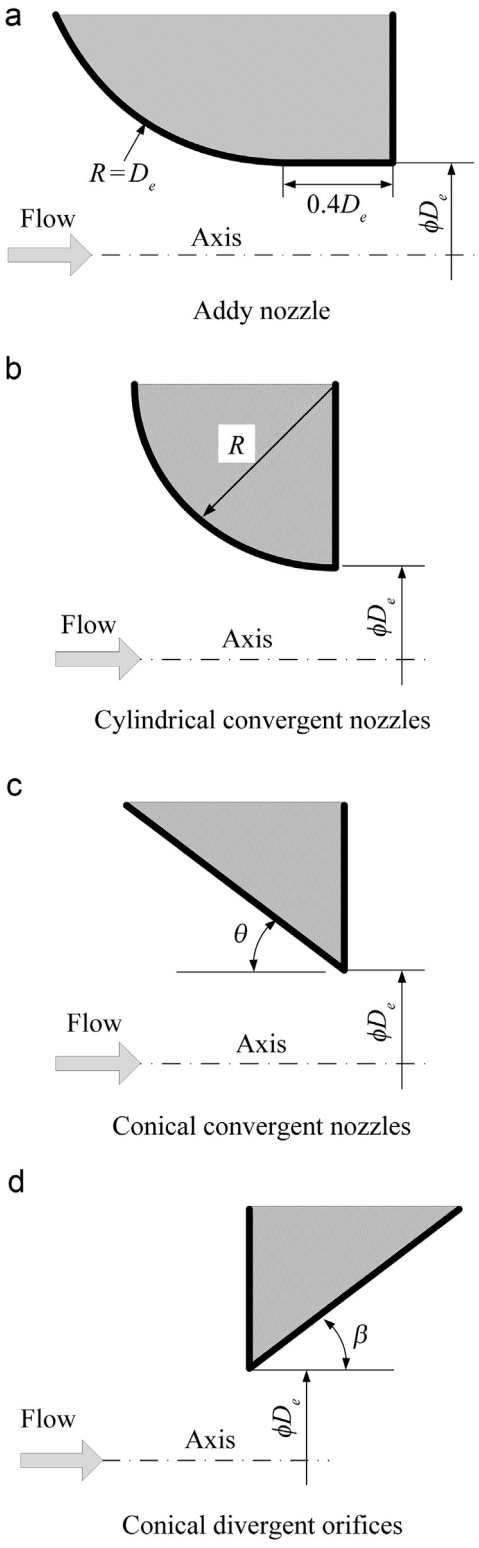

Figure 2 Schematics of nozzle configurations. (a) Addy nozzle, (b) cylindrical convergent nozzles, (c) conical convergent nozzles, and (d) conical divergent orifices.

Table 1 Detailed about various nozzle configurations.

Nozzle types	Description	
Addy nozzle	Circular arc, $R=D_e$; straight$=0.4D_e$	
		$R/10^{-3}$ m
Cylindrical convergent nozzles	6*R*	6
	12*R*	12
	18*R*	18
	24*R*	24
	30*R*	30
		θ/degree
Conical convergent nozzles	30*T*	30
	45*T*	45
	60*T*	60
	75*T*	75
		β/degree
Conical divergent orifices	30*D*	30
	35*D*	35
	40*D*	40
	45*D*	45
	50*D*	50
	60*D*	60
	75*D*	75
	90*D*	90

(4) Conical divergent orifices with divergence angles $\beta=30°$, 35°, 40°, 45°, 50°, 60°, 75° and 90° (Figure 2(d)).

The detail information about these nozzle inlet configurations are presented in Table 1. The nominal diameter of the nozzle exit and orifice in all cases was kept constant at $D_e=12.7\times10^{-3}$ m (characteristics length). The symbolic representations for various nozzles as presented in Table 1 were used in the discussion for convenience.

Dry air as working fluid was driven at Reynolds number of $Re=5.92\times10^5$ through the nozzles. The nozzle pressure ratio p_0/p_b (ratio of total pressure p_0 to the back pressure p_b) was kept constant at 6.2. The upstream total temperature T_0 and total pressure p_0 were maintained constant at 298.15 K and 101.3 kPa, respectively, through the whole computations. The boundary conditions used were the inlet total pressure and the outlet static pressure at the upstream and downstream of the computational domain, respectively. The symmetric conditions at the axis of the nozzle were used to reduce the computational effort for the full domain, and the adiabatic no-slip conditions were applied to the solid walls.

To ensure the computational domain independent solutions, the upstream domain was extended to the distance of $100D_e$ upstream from the nozzle exit, and the downstream was extended to the distance of $100D_e$ and $50D_e$ in the *x*- and *r*-directions, respectively. A structured grids system was employed in computations. The typical grids system employed in the present computation is shown in Figure 1. Several preliminary computations have been performed with different sizes of mesh to investigate the grid dependence of the solution. The location L_m and diameter D_m of Mach disk were calculated for those grids systems. The calculated

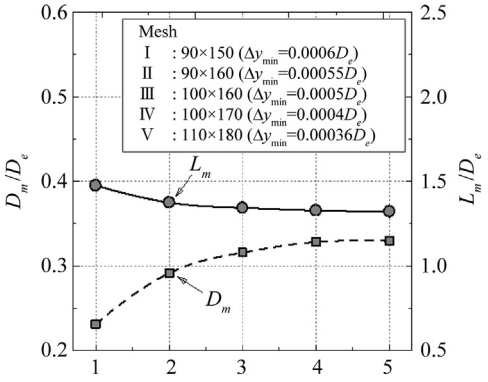

Figure 3 Mesh dependency test results.

results for five representative meshes are shown in Figure 3. Here, the data of location L_m and diameter D_m of Mach disk are normalized by the nozzle exit diameter D_e and $\Delta y_{\min}$ represents the grids closest to the wall. Based on these results, the type IV mesh which was used for the simulations is the suitable and economic one to simulate the problem. The grids in type IV mesh are 70 in $\times$ 80 in the nozzle region and 100 in $\times$ 170 in the jet plume region and $\Delta y_{\min}$ are located at $0.0004D_e$ away from the wall. The grids were densely clustered in the boundary layers in order to provide more reasonable predictions.

A solution convergence was obtained when the residuals for each of the conserved variables were reduced below the order of magnitude 4. Another convergence criterion was to check the conserved quantities directly through the computational boundaries. The net mass flux was investigated when there was an applicable imbalance through the computational boundaries.

3. Results and discussion

3.1. Comparison with the experimental results

The validation of the present computational work was carried out through a comparison of the computed underexpanded supersonic free jets with our experimental results [24]. In both experiment and numerical works jets were issued from the cylindrical straight nozzle [23]. The range of pressure ratio p_0/p_b was varied between 3.8 and 6.2. The upstream total temperature T_0 and pressure p_0 in the numerical study were the same as that with the experiment, and values were 298.15 K and 101.3 kPa, respectively.

Figure 4 shows a comparison of the computed iso-density contours with the shadowgraph pictures of underexpanded supersonic jets. The jet at $p_0/p_b=3.8$ is slightly underexpanded (see Figure 4(a)), and the resulting weak shock waves that have the regular reflection at point 'P'. While the jet flow at $p_0/p_b=6.2$ is strongly underexpanded at the nozzle exit compared with the case shown in Figure 4(a), and barrel shocks are formed due to the difference in pressures between the underexpanded and ambient gases. These shocks reflect on

the jet axis. Consequently, Mach disk is formed near the jet axis. At the interaction of Mach disk with barrel shock, a triple-point is formed. In the downstream of the triple point the slip line is observed. As the pressure ratio increases, the shock cells extend stream-wise that result in an increase of the length of supersonic core of jets. The predicted iso-density contours are nearly the same as the results obtained by the experiment. In addition, the present computations predicted the diameter and location of Mach disk to be 0.515 and 1.526, respectively, while the experimental values are 0.521 and 1.545, respectively. Thus, it can easily be mentioned that the present computations predicted the jet and shock structures of under-expanded supersonic jets with a good accuracy.

3.2. *Discharge coefficients and sonic lines*

The discharge coefficient C_d is an important characteristics of a nozzle. It is defined as the dimensionless ratio of the actual mass flow rate to the ideal mass flow rate corresponding to one-dimensional isentropic flow for the same upstream stagnation conditions, and is given by,

$$C_d = \frac{\dot{m}_{act}}{\dot{m}_{ideal}} \tag{18}$$

In the equation, $\dot{m}_{ideal}$ for an ideal compressible gases flow through cylindrical and conical convergent nozzles can be calculated as follows [25]:

$$\dot{m}_{ideal} = \frac{A_e p_0}{\sqrt{T_0}} \sqrt{\frac{\gamma}{\Re}} M \left(1 + \frac{\gamma - 1}{2} M^2\right)^{-\frac{\gamma+1}{2(\gamma-1)}} \tag{19}$$

Whilst $\dot{m}_{ideal}$ for an ideal gases through conical divergent orifices can be estimated by the following equation [26].

$$\dot{m}_{ideal} = A_e \sqrt{2\rho_0 p_0 \left(\gamma/(\gamma-1)\right)\left[\left(p/p_0\right)^{2/\gamma} - \left(p/p_0\right)^{(\gamma+1)/\gamma}\right]} \tag{20}$$

where, A_e is the area at nozzle exit, $\Re$ is the gas constant, γ is the ratio of specific heats, M is the flow Mach number, p is the pressure and T is the temperature. Subscript 0 refers to the stagnation condition. The mass flow rate is a maximum for nozzles at chocked condition ($M=1$). The discharge coefficient differs from unity due to the nonuniformity of flow parameters (such as Mach number) at the nozzle exit and presence of boundary layer (viscous effect).

The computed discharge coefficients for cylindrical, conical convergent nozzles and conical divergent orifices are plotted against the radius of curvatures R, convergent angles θ and divergent angles β, respectively, in Figure 5. Here, it is mentioned that the discharge coefficient for Addy nozzle is presented in the figure as reference. For cylindrical convergent nozzles, the discharge coefficient increases along with R in the range of small R (≤ 18 mm) but the variation decreases in the range of large R (≥ 18 mm). For conical convergent nozzles with sharp corner at exit, the discharge coefficient significantly decreases with the increase of convergent angles θ, and it can be given by a linear decay function of θ. It indicates that the performance

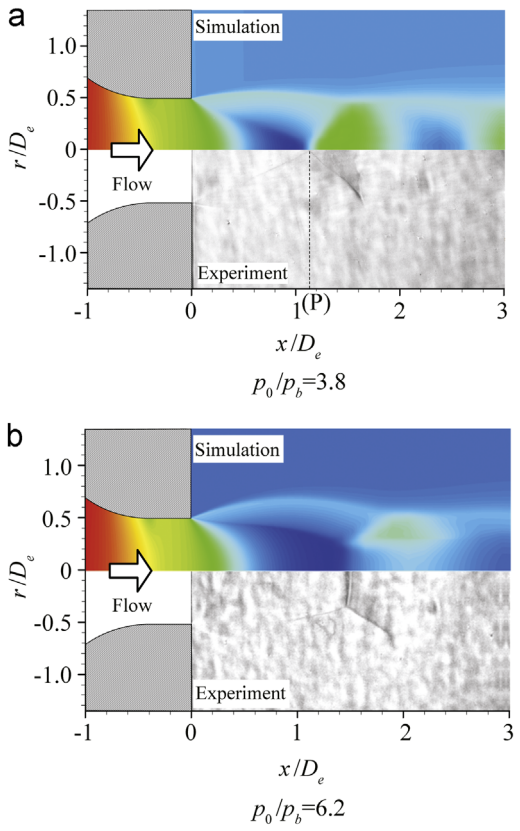

Figure 4 Comparison of computed iso-density contours with the experimental results. (a) $p_0/p_b=3.8$ and (b) $p_0/p_b=6.2$.

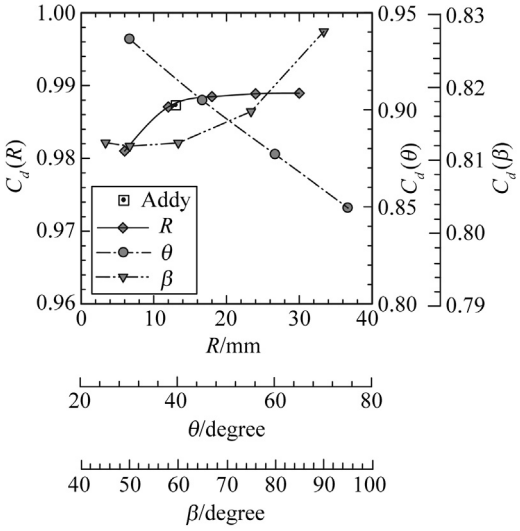

Figure 5 Discharge coefficients for nozzle with varying geometries.

of conical convergent nozzles with small conical angles θ is preferably higher than those with large angles θ. Whilst C_d for conical divergent orifices increase almost linearly with the increase of divergent angles β in the range of $60^\circ < \beta \leq 90^\circ$, and the effect of divergent angles β is insignificant on discharge coefficient in the range of $45^\circ < \beta \leq 60^\circ$. The results C_d for $\beta = 30^\circ$, 35° and 40° are

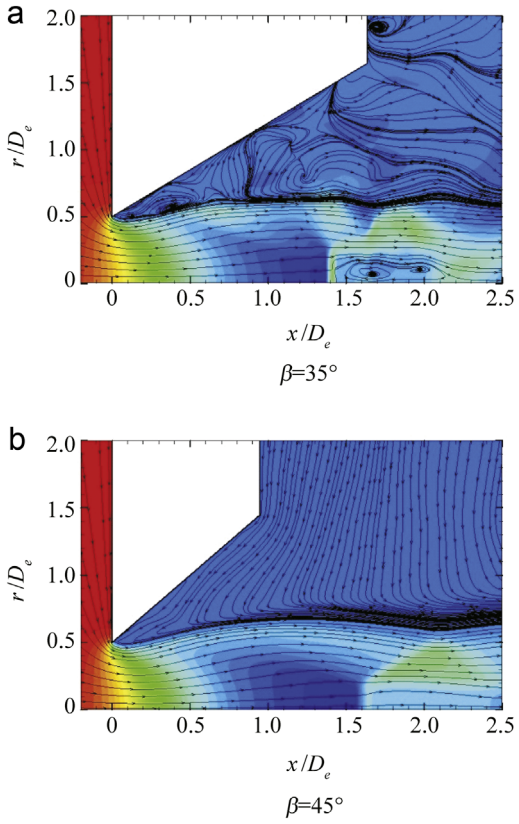

Figure 6 Density contours and streamlines for conical divergent orifices. (a) $\beta=35^\circ$ and (b) $\beta=45^\circ$.

not presented here in the present discussion, though we have conducted studies on them.

The entrainment flows downstream of the divergent orifices are restricted at small divergent angles $\beta=30^\circ$, 35° and 40°, and this phenomenon can clearly be visualized through the computed density contours and streamlines for conical divergent orifice with $\beta=35^\circ$ presented in Figure 6 (a). Besides, for $\beta=45^\circ$ and on ward, the entrainment flow comes contact with the flow issuing from the orifice, and that results in the correct formation of jet and shock structures, as shown in Figure 6(b). Thus, the results presented in the paper only for cases of fully developed flows ($\beta=45^\circ$, 50°, 60°, 75° and 90°) regardless of considering the effect of divergent angles on the downstream flows.

In order to examine the effect of flow parameter such as Mach number at nozzle exit on the discharge coefficient, the computed profiles of sonic lines for cylindrical, conical convergent nozzles and divergent orifices are illustrated in Figure 7(a), (b) and (c), respectively. For cylindrical convergent nozzles, sonic lines are curvilinear, and they are notably influenced by the radius R. The sonic line for $R=6$ mm is placed significantly downstream of the nozzle exit, whereas the sonic line moves upstream as R increases. For Addy nozzle, the profile of sonic line in viscous flow reaches downstream of the nozzle exit, whereas the inviscid

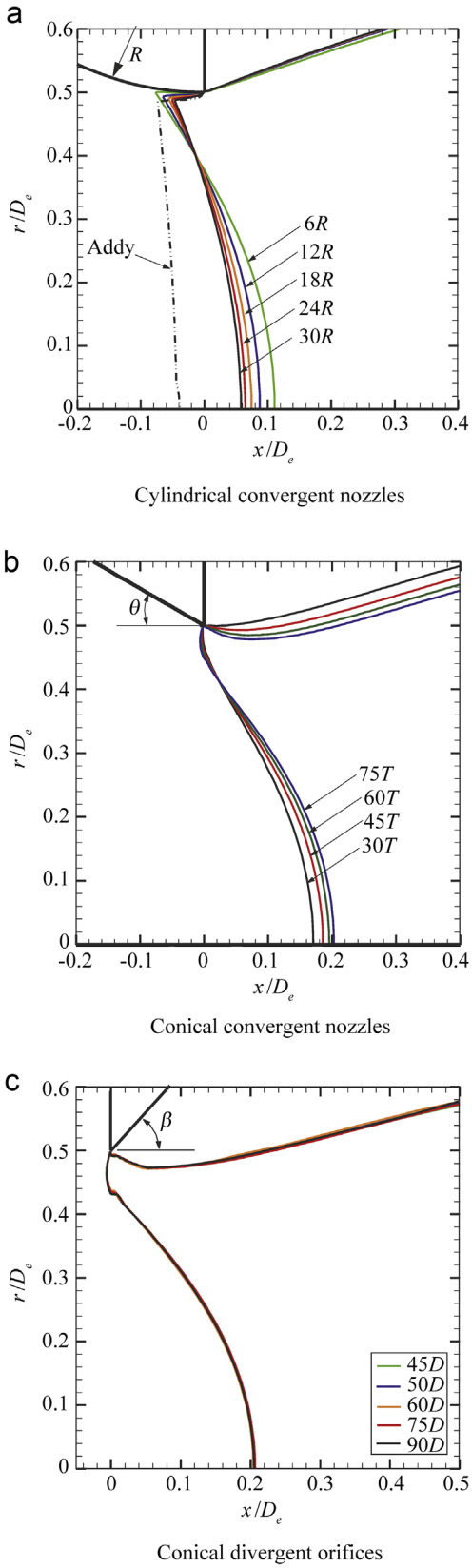

Figure 7 Sonic lines for nozzle with varying geometries. (a) Cylindrical convergent nozzles, (b) conical convergent nozzles, and (c) conical divergent orifices.

profile approaches to the nozzle exit. The viscous effect is dominant in the straight part of the Addy nozzle [23] and that effect can clearly be noticed from the distribution of boundary layer thickness near nozzle exit in Figure 8. The boundary layer occupy a sizeable portion of the nozzle cross-section and acts like a converging–diverging section which leads to shift virtual throat of this converging–diverging section to some upstream location from the nozzle exit.

The profile of sonic lines for conical convergent nozzles as shown in Figure 7(b) exhibit point of inflection and the flow nonuniformity may be substantial and it grows with increase of the convergent angle θ. The sonic line trends towards the downstream direction with the angle θ. Besides, the influence of divergent angles β on the sonic line profiles are insignificant for conical divergent orifices. The sonic lines are intersect with the axis about an axial location of x/D_e=0.2 downstream of the nozzle exit, and the profile shown in Figure 7(c) displays point of inflection in the same fashion like conical convergent nozzles.

The inflection of sonic lines for conical convergent nozzles and divergent orifices is measured through an angle α. The α is calculated as described in the typical schematic diagram that illustrated in Figure 9. The computed angles of inflection α for conical convergent nozzles and divergent orifices then graphed against convergent and divergent angles θ and β in Figure 10(a) and (b), respectively. The inflection angles α in both cases of conical convergent nozzles and divergent orifices can be given by linear growth functions of θ and β, respectively, as follows.

$$\alpha\,(\text{deg}) = 0.1696 \times \theta\,(\text{deg}) + 3.7763 \tag{21}$$

and

$$\alpha\,(\text{deg}) = 0.041 \times \beta\,(\text{deg}) + 10.97 \tag{22}$$

In addition, the increment of the inflection angle α for conical convergent nozzles is higher compared with the case of conical divergent orifices.

3.3. *Effects on the aerodynamic features of jets*

The configuration of jet boundaries of supersonic jets issuing from cylindrical, conical convergent nozzles and divergent orifices are computed and presented graphically in Figure 11(a), (b) and (c), respectively. The location of jet

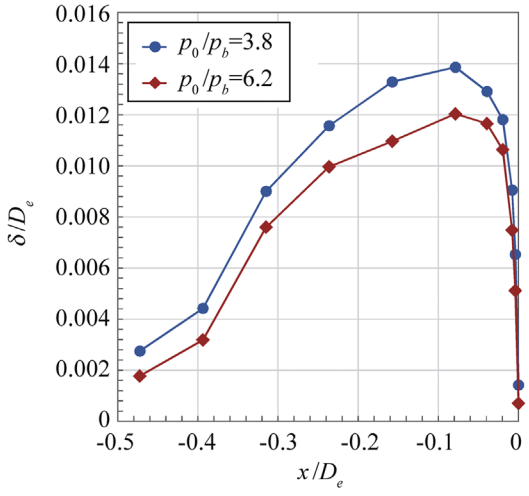

Figure 8 Distributions of boundary layer thickness near the exit of Addy nozzle.

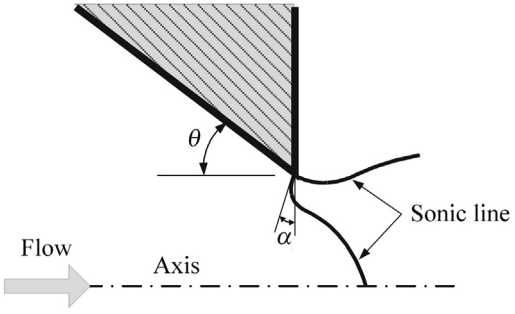

Figure 9 Schematics of sonic line inflection for conical convergent nozzles.

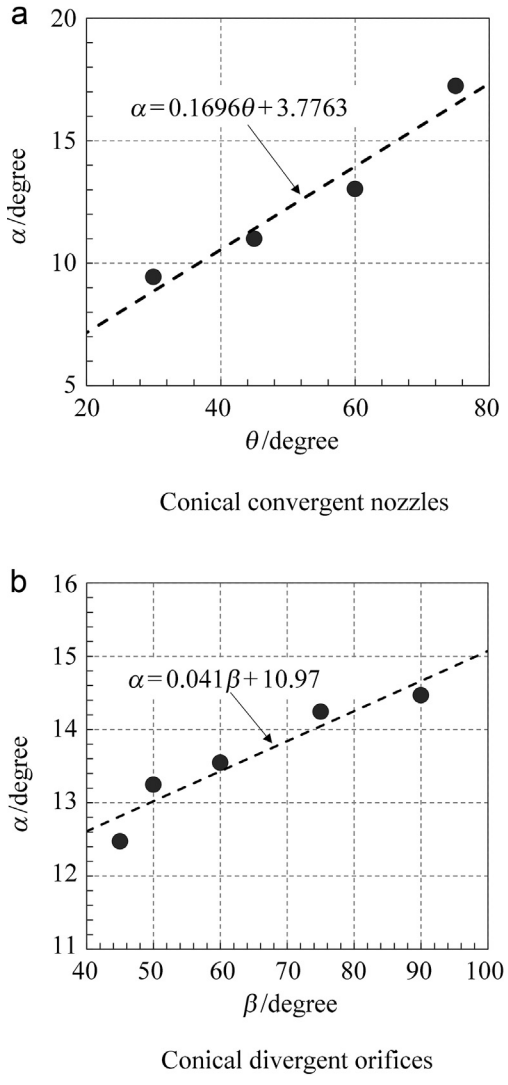

Figure 10 Inflection of sonic lines for conical convergent nozzles and divergent orifices. (a) Conical convergent nozzles and (b) conical divergent orifices.

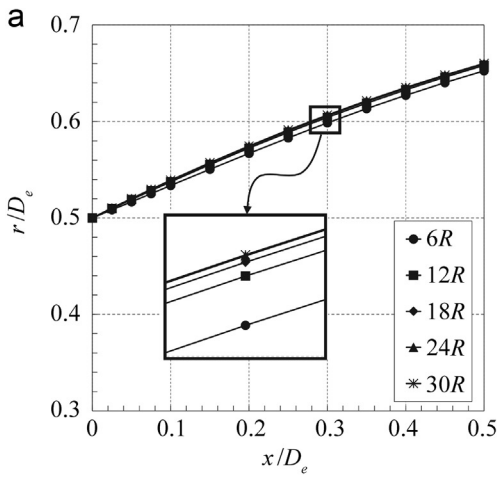

Cylindrical convergent nozzles

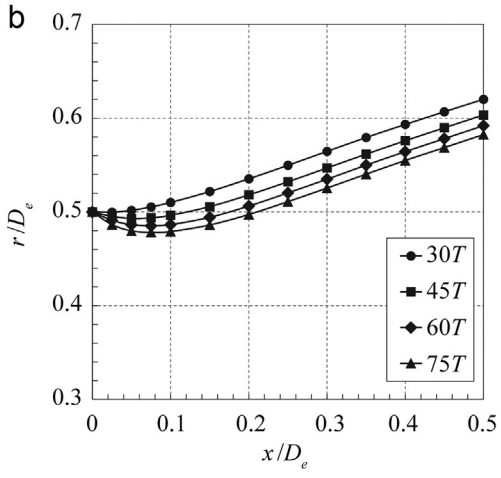

Conical convergent nozzles

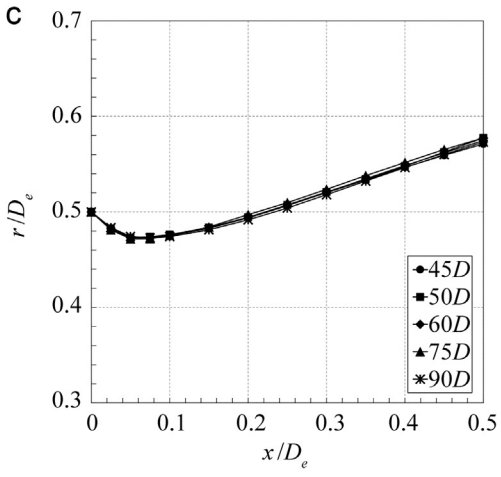

Conical divergent orifices

Figure 11 Jet boundaries for cylindrical, conical convergent nozzles and divergent orifices. (a) Cylindrical convergent nozzles, (b) conical convergent nozzles, and (c) conical divergent orifices.

boundary is defined with the largest value of density gradient ($d\rho/dr$) on an arbitrary cross section normal to x-axis. The radius of curvature R and divergent β in cylindrical convergent nozzles and conical divergent orifices exhibit no salient influence on the configuration of jet boundaries shown in Figure 11(a) and (b), respectively. Whereas, the present computed data for conical convergent nozzles shows that the jet boundary trends to shrink inward with the increase in the convergent angles θ, as shown in Figure 11(b). In addition, comparing the configuration of jet boundaries for conical convergent nozzles and divergent orifices the inward inflection of jet boundary is large for divergent orifices. It indicates that the inward inflection is dependent on the nozzle geometry.

For conical convergent nozzles and divergent orifices, since the presence of curvilinear sonic lines result in the dependence of the critical pressure drop on the value of convergent and divergent angles θ and β, respectively. To make a clear insight about this flow physics, we investigated efflux of a gas from conical convergent nozzles and divergent orifices. A schematic view of efflux from a conical convergent nozzle is shown in Figure 12. From the schematic diagram, it can be seen that the maximum contraction takes place at finite distance of l_0 slightly downstream of the nozzle exit, where the jet is more or less horizontal. At this section, the cross-section area of fluid stream is minimum, streamlines are almost parallel and the pressure drop across the jet is constant. This section is called as vena contracta. The reason for this phenomenon is that fluid streamlines cannot abruptly change direction. In the free jet, the streamlines are unable to closely follow the sharp change of angle in the nozzle wall. The converging streamlines follow a smooth path, which results in the narrowing of the jet observed.

The position of vena contracta l_0 from the exit was computed and the data for the conical convergent nozzles and divergent orifices are plotted against the convergent and divergent angles θ and β in Figure 13(a) and (b). In these cases, the distance l_0 increases with the increase of θ and β and can be given by the linear functions those are presented in figures. For conical convergent nozzle, the slope of the linear function is large compared with that of conical divergent orifices.

The shear layer in supersonic jets is one of the fundamental characteristics of supersonic mixing layers. Since there exists expansion and compression waves in the jet

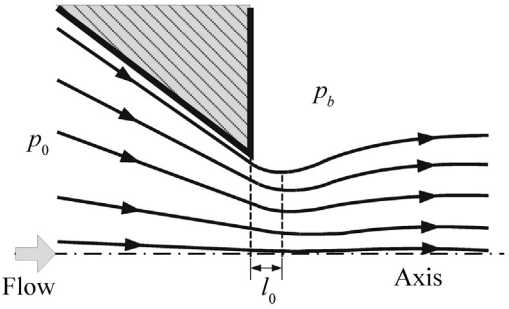

Figure 12 Schematics of the efflux from conical convergent nozzles.

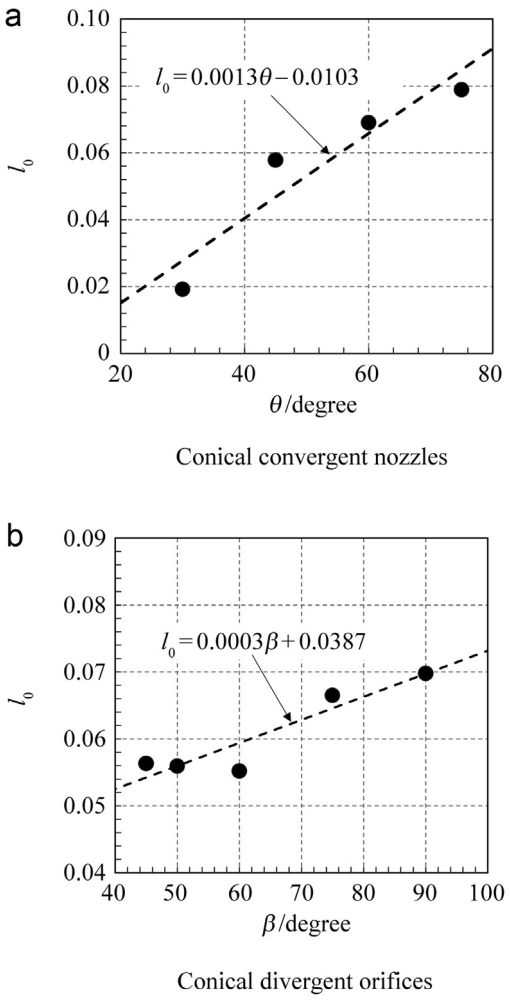

Figure 13 Distributions of l_0 for conical convergent nozzles and divergent orifices. (a) Conical convergent nozzles and (b) conical divergent orifices.

flowfield the exact estimation of the shear layer thickness is very important. Hence, the definition of shear layer thickness using the 95%–5% criteria is applied to the cross-stream pressure data, and the measured of shear layer thickness δ_{sh} as function of axial distance x/D_e from the nozzle exit is presented in Figure 14(a), (b) and (c) for cylindrical, conical convergent nozzles and divergent orifices, respectively.

The thickness δ_{sh} is normalized by the nozzle exit diameter D_e. The plot for cylindrical convergent nozzles, in Figure 14(a), suggests that the shear layer near nozzle exit ($x/D_e \leq 0.15$) is significantly influenced by the radius of curvatures R, and the thickness decreases with the increase of R in this near exit region. Away from the exit ($x/D_e \geq 0.15$) the thickness δ_{sh} follows fairly linear growth. Whilst, from Figure 14(b) and (c), the influence of convergent and divergent angles θ and β, respectively, on the growth of shear layer is insignificant, and the shear layer grow linearly along the axial direction. The growth rate of

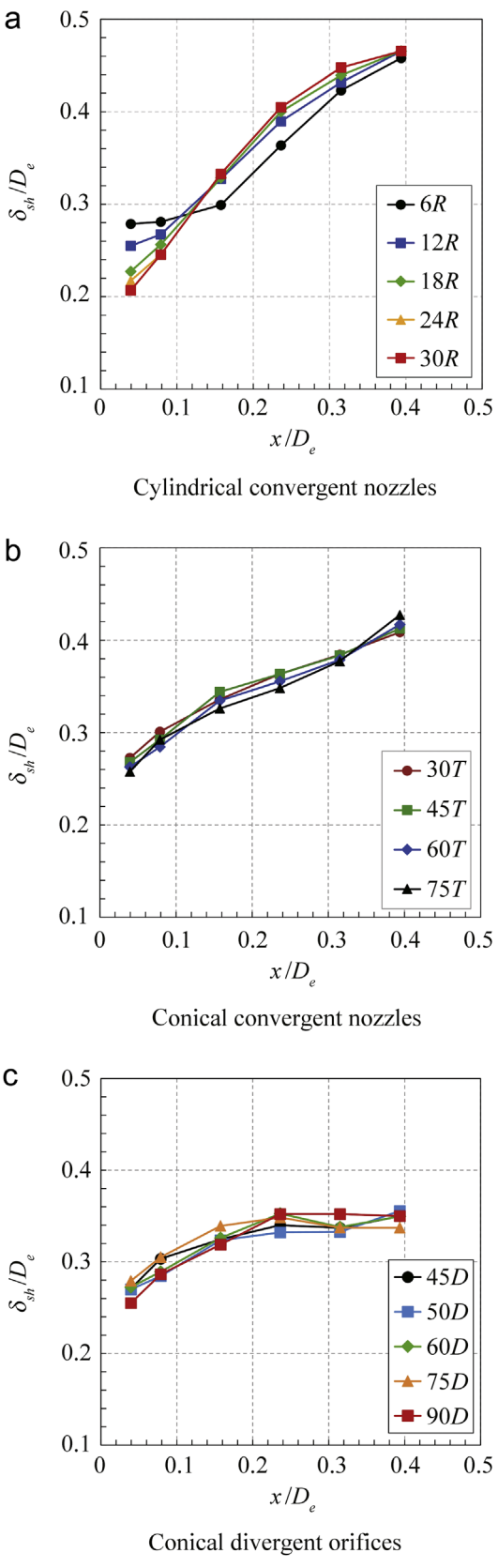

Figure 14 Distributions of shear layer thickness for conical convergent nozzles and divergent orifices. (a) Cylindrical convergent nozzles, (b) conical convergent nozzles, and (c) conical divergent orifices.

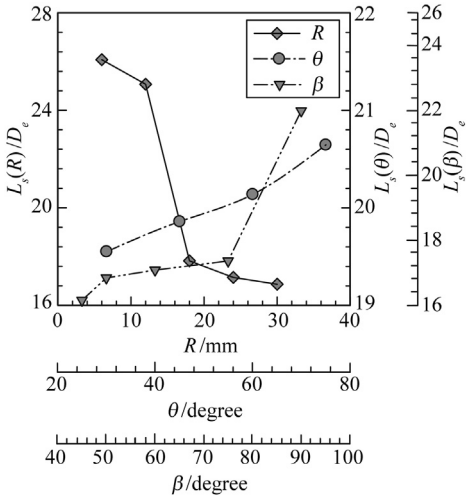

Figure 15 Supersonic core lengths of jets issuing from nozzles with varying geometries.

shear layer is slower for conical divergent orifices compared with that of conical convergent nozzles.

The length of supersonic core is the measure of physical size of the jet. This length is determined by the axial point farthest downstream at which there exists a flow Mach number of unity. The computed supersonic core lengths L_s for cylindrical, conical convergent nozzles and divergent orifices are graphically plotted against the radius of curvatures R, convergent angles θ and divergent angles β in Figure 15. For cylindrical convergent nozzles the length L_s is greatly affected by the radius R, and L_s decreases with the increase of R. The length L_s for conical convergent nozzles, on the other hand, can be given by a linear growth function of convergent angles θ. Whilst the supersonic core lengths L_s for conical divergent orifices increases linearly with smaller slope in the range of divergent angles $\beta \leq 75^\circ$ and beyond this range ($\beta > 75^\circ$) a rapid increment of the length L_s is observed.

4. Conclusions

The present work dealt with the numerical simulations of viscous turbulence flows through nozzles with varying geometry. Compressible RANS equations were solved along with SST k–ω turbulence model. The computational code was validated through comparison of the numerical results with the experimental data. Several cylindrical, conical convergent nozzles and divergent orifices with varying radius of curvatures, convergent and divergent angles, respectively, were used to investigate the geometry effect on the nozzle performance in terms of the discharge coefficient. Investigating the effect of flow parameters at nozzle exit the sonic lines and their inflection were analyzed. The discharge coefficient significantly influenced by the radius of curvatures, convergent and divergent angles. The sonic line moved towards nozzle exit as the radius of curvature increased, while it trend towards the downstream direction with the increase of convergent angle. The influence of divergent angles on the profile of sonic lines was insignificant. The inflection of sonic line found increasing with the increase of convergent and divergent angles. Significant influence of nozzle geometry was noticed on the configuration of jet boundaries, shear layers and lengths of supersonic core of jets. The geometry effect on jet boundaries was dominant for conical convergent nozzles, and the jet boundary showed a trend to shrink inward with the increase of convergent angles. However, the influence of convergent and divergent angles for conical convergent nozzles and divergent orifices, respectively, on the shear layer was insignificant. The length of supersonic core decreased with the increase of radius of curvatures, and increased with the increase of convergent and divergent angles. Finally, these findings surely could play important role in designing nozzles that are widely using in a variety of engineering applications.

References

[1] E.S.Love, D.E. Grigsby, L.P. Lee, M.J. Woodling, Experimental and theoretical studies of axisymmetric free jets, NASA TR R-6, 1959.

[2] W. Sheeran, D. Dosanjh, Observations on jet flows from a two-dimensional, underexpanded, sonic nozzle, AIAA J. 6 (3) (1968) 540–542.

[3] S.G.E.A. Meier, W.C. Selerowicz, A.P. Szumowski, A nozzle generating low jet noise, J. Sound Vibr. 136 (1990) 65–73.

[4] P. Birkby, G.J. Page, Numerical predictions of turbulent underexpanded sonic jets using a pressure-based methodology, J. Mech. Eng. 215 (2001) 165–173.

[5] M. Ishibashi, M. Takamoto, Discharge coefficient of super-accurate critical nozzle at pressurized condition, in: Proceedings of the 4th International Symposium of Fluid Flow Measurement, Denver, USA, June 1999.

[6] H. Dietrich, B. Nath, E. von Lavante, High accuracy test rig for gas flows from 0.01 m^3/h up to 25000 m^3/h, in: Proceedings of the International Measurement Confederation (IMEKO-XV) Congress, Osaka, Japan, June 1999.

[7] M. Ishibashi, M. Takamoto, Very accurate analytical calculation of the discharge coefficient of critical venturi nozzles with laminar boundary layer, in: Proceedings of International Symposium on Fluid Control, Measurement and Visualization (FLUCOME), Hayama, Japan, September 1997.

[8] S. Som, A.I. Ramirez, D.E. Longman, S.K. Aggarwal, Effect of nozzle orifice geometry on spray, combustion, and emission characteristics under diesel engine conditions, Fuel 90 (3) (2011) 1267–1276.

[9] R. Payri, F.J. Salvador, J. Gimeno, J. de la Morena, Effects of nozzle geometry on direct injection diesel engine combustion process, Appl. Therm. Eng. 29 (10) (2009) 2051–2060.

[10] S. Matsuo, M. Tanaka, Y. Otobe, H. Kashimura, H.D. Kim, T. Setoguchi, Effect of axisymmetric sonic nozzle geometry on characteristics of supersonic air jet, J. Therm. Sci. 13 (2) (2004) 121–126.

[11] Y. Otobe, H. Kashimura, S. Matsuo, T. Setoguchi, H.D. Kim, Influence of nozzle geometry on the near-field structure of a

highly underexpanded sonic jet, J. Fluids Struct. 24 (2008) 281–293.
[12] N. Menon, B.W. Skews, Effect of nozzle inlet geometry on underexpanded supersonic jet characteristics, in: Proceedings of 26th International Symposium of Shock Waves, Germany, July 15–20, 2007.
[13] K. Hatanaka, T. Saito, Influence of nozzle geometry on underexpanded axisymmetric free jet characteristics, Shock Waves 22 (2012) 427–434.
[14] Y. Yu, M. Shademan, R.M. Barron, R. Balachandar, CFD study of effects of geometry variations on flow in a nozzle, Eng. Appl. Comput. Fluid Mech. 6 (3) (2012) 412–425.
[15] S.K. Hebber, K. Sridhara, P.A. Paranjpe, Performance of conical jet nozzles in terms of discharge coefficient, J. Aeronaut Soc. India 22 (1) (1970) 3–9.
[16] A. Cruz-Mava, F. Sánchez-Sllva, P. Qulnto-Dlez, M. Toledo-Velázquez, Characterization of the discharge coefficient of a sonic venture nozzle, J. Appl. Res. Technol. 3 (2) (2005) 104–117.
[17] ANSYS Inc., Fluent User's guide, 2011, USA.
[18] F.R. Menter, Zonal two equation k-ω turbulence models for aerodynamic flows, AIAA Paper 93-2906, 1993.
[19] F.R. Menter, Two-equation eddy-viscosity turbulence models for engineering applications, AIAA J. 32 (1994) 269–289.
[20] F.R. Menter, M. Kuntz, R. Langtry, Ten years of industrial experience with the SST turbulence model, in: K. Han-Jalic, Y. Nagano, M. Tummers (Eds.), Turbulence, Heat and Mass Transfer, 4, Begell House Inc., 2003, pp. 625–632.
[21] P.L. Roe, Approximate Riemann solvers, parameter vectors, and difference schemes, J. Comput. Phys. 43 (1981) 357–372.
[22] B. van Leer, Towards the ultimate conservative difference scheme V: a second order sequel to Godunov's method, J. Comput. Phys. 32 (1979) 101–136.
[23] A.L. Addy, Effects of axisymmetric sonic nozzle geometry on Mach disk characteristics, AIAA J. 19 (1981) 121–122.
[24] M.M.A. Alam, S. Matsuo, T. Setoguchi, Effect of non-equilibrium homogeneous condensation on the self-induced flow oscillation of supersonic impinging jets, Int. J. Therm. Sci. 49 (2010) 2078–2092.
[25] P.H. Oosthuizen, Compressible Fluid Flow, 1st edition, McGraw-Hill Science, USA, 1997.
[26] Handbook of Chemical Hazard Analysis Procedures, Appendix B, Federal Emergency Management Agency, U.S. Dept. of Transportation, and U.S. Environmental Protection Agency, 1989.